PIER C

(Received 7 April 2025, Accepted 16 May 2025, Scheduled 26 May 2025)

A Defect Scanning Sensor Based on a Reconfigurable Spiral-Shaped DGS

Zhi Chen*

School of Information Science and Engineering, Zhejiang Sci-Tech University, Hangzhou, Zhejiang, China

ABSTRACT: Microwave non-destructive testing (NDT), with its high sensitivity and non-contact advantages, is widely applied in the defect detection of non-metallic composite materials. However, conventional microwave NDT requires frequently mechanical moving to modify the detection area, significantly reducing the detection efficiency. To address this limitation, this paper proposes a reconfigurable spiral defect-ground structure (DGS)-based defect scanning sensor. The sensor is loaded with multiple spiral DGS units, with PIN diodes bridged across them. By switching the state of the diodes electronically, the area of the electric field concentration is changed, furthermore controlling the sensitive detection area without mechanical movement. Compared to the existing complementary split-ring resonator (CSRR) sensors, which have a unit detection area of 3 mm × 3 mm, the proposed sensor achieves an enhanced unit detection area of 15.5 mm × 11 mm. Additionally, relying on the unique structural characteristics of the spiral shape, the field distributes more evenly, effectively reducing blind spots in detection. Experimental results demonstrate that the proposed reconfigurable spiral DGS-based defect scanning sensor can effectively detect defects in non-metallic composite materials.

1. INTRODUCTION

Non-metallic composite materials, known for their light weight, high strength, and ease of processing, are widely utilized in fields such as aerospace energy [1]. In industrial applications, non-metallic composites are prone to internal defects due to factors such as usage wear and fatigue accumulation, which significantly affect their reliability in practice and increase safety risks seriously. Hence, defect detection in non-metallic composites is significant [2].

Several detection methods have been proposed by many researchers. Ultrasonic testing [3] relies on a coupling agent for surface contact, limiting its applicability in certain scenarios; radiographic testing [4–6] not only incurs high costs but may also poses health risks to operators; thermal imaging testing [7, 8] involves a heating process that not only increases detection time but also makes the accuracy of results susceptible to environmental factors such as temperature. By contrast, microwave technology, owing to its ability to penetrate dielectric materials, offers a promising approach for defect detection by analyzing variations in microwave parameters. As a result, microwave non-destructive testing has gained widespread attention from researchers and is applied in defect detection of non-metallic composites due to its non-contact nature, high integration, and durability [9].

In recent years, various types of microwave non-destructive testing sensors have been designed and applied to defect detection [10–12]. For instance, waveguide sensors [13] have been employed to detect defects in ceramic materials. However, their sensitivity depends on the operating frequency, and higher frequencies are associated with increased costs. In addition, the use of reflection methods for defect detection often requires expensive specialized equipment [14]; a flexible sensor based on Spoof Surface Plasmon Polaritons (SSPPs) [15] was proposed for defect detection, but its detection area is confined to a fixed region. Introduced by Pendry et al. in 1999, Split-Ring Resonator (SRR) structure is an artificial structure [16]. Due to its high sensitivity, SRR-based sensors have found widespread application [17–19], leading to the development of various derivative structures, among which Complementary Split-Ring Resonator (CSRR) [20–22] is one of the most representative. CSRR structure concentrates electromagnetic field within the gap of the split ring, and while it offers high sensitivity, it leads to uneven electric field distribution inherently.

Because of the constrained detection range of CSRR structure, frequent mechanical movement across the surface of the object being tested is required, which substantially diminishes detection efficiency. To overcome this limitation, researchers have put forward methods to control the switching of the sensor's detection area for defect inspection electronically. By controlling the diodes loaded between the inner and outer rings of the SRR, the sensor's detection area can be electronically shifted along a specific direction [23]. However, in practical testing, the detection area of a single unit is only 3 mm × 3 mm, and frequent transitions between multiple sensor units further reduce detection efficiency [24].

This paper reveals a defect scanning sensor based on a reconfigurable spiral DGS for detecting defects in non-metallic composite materials by monitoring frequency shifts [25]. Leveraging the spiral structure, the electric field distribution in the detection area is more uniformly, thereby reducing detection blind spots. Additionally, the sensor loads multiple spiral DGS detection units, with PIN diodes used to dynamically reconfigure the sensor across different units, thus controlling the sensitive

* Corresponding author: Zhi Chen (a3197974817@163.com).

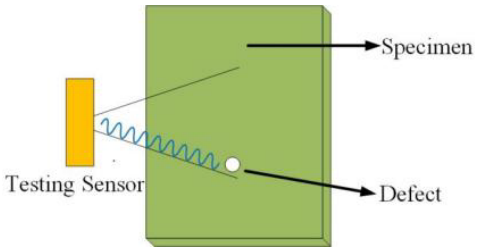

FIGURE 1. Microwave NDT schematic.

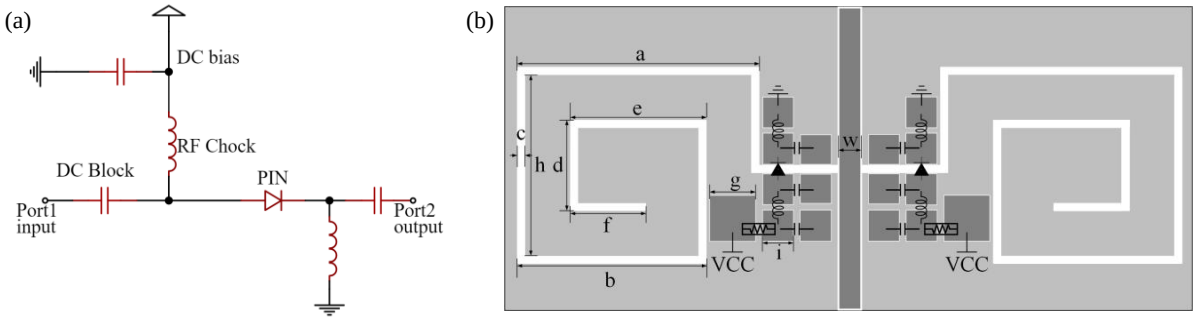

FIGURE 2. Schematic diagram of the sensor: (a) Bias circuit; (b) Proposed sensor layout based on spiral DGS.

detection area without moving. Compared to previous research, the sensor proposed significantly expands the detection area of each unit and reduces the switching frequency through electronic control, increasing detection speed substantially.

2. THE PRINCIPLE OF THE RECONFIGURABLE DEFECT STRUCTURE

Microwave NDT exploits the interaction between microwaves and the electromagnetic properties of the material under inspection. The presence of defects leads to variations in the dielectric constant, which in turn affects the propagation of the microwaves. The phenomena such as reflection, transmission, and scattering occur as the microwaves propagates, causing interference effects. These interactions result in measurable changes in signal parameters such as amplitude and frequency, enabling the detection and characterization of internal structural defects within the material consequently. A schematic diagram of the principle is shown in Figure 1.

Based on the basic principle of microwave nondestructive testing, we have designed this sensor. Figure 2(a) shows the biasing circuit of the PIN diode in the sensor. By controlling the state of the diode, a reconfigurable design of the sensor can be achieved. The schematic diagram of the sensor is shown in Figure 2(b).

The sensor features a spiral structure etched onto the metal ground plane of the microstrip line, with the dielectric substrate remaining unchanged and maintaining its original dielectric material. The PIN diode, as shown in Figure 2(a), is incorporated at the top layer of the sensor, bridging the DGS to function as a switch. The dimensional parameters of the sensor are as follows: $a = 15.5\,\text{mm}$, $b = 12.5\,\text{mm}$, $c = 0.5\,\text{mm}$, $d = 3.3\,\text{mm}$, $e = 8.5\,\text{mm}$, $f = 4.5\,\text{mm}$, $g = 3\,\text{mm}$, $h = 10\,\text{mm}$, $i = 2\,\text{mm}$, $w = 1.5\,\text{m}$. The resistance values are all $1\,\text{k}\Omega$; the capacitance values are all 100 pF; the inductance values are all 22 nH; and the supply voltage (VCC) is 3.3 V.

To demonstrate how the aforementioned PIN diode enables reconfigurability, we have simulated the transmission coefficient (S_{21}) of the sensor under two states of the PIN diode: forward bias (off) and reverse bias (on), as shown in Figure 3. The model's dimensional parameters remain consistent with those in Figure 2(b). The dielectric substrate material used in the simulation is FR4, with a substrate thickness of 1 mm, a relative permittivity of 4.4, and a loss tangent of 0.02. The electromagnetic simulation was performed in High Frequency Structure Simulator (HFSS).

As shown in Figure 3, when the switch is in the off state, a significant transmission zero appears at 0.89 GHz. This transmission zero can be equivalently modeled as the LC parallel resonance frequency in the circuit model shown in Figure 4. At the resonance frequency, the transmission effect is nearly zero, resulting in a prominent lower bound in Figure 3. When the switch is closed, the DGS is approximately in a short-circuit state, and the signal can be approximated as passing through without obstruction within the observed frequency range.

In this equivalent circuit model, the calculations for the inductance and capacitance are as follows:

$$C = \frac{\omega_c}{2Z_0(\omega_0^2 - \omega_c^2)} \tag{1}$$

$$L = \frac{1}{4\pi^2 f_0^2 C} f_0 \tag{2}$$

where ω_0 is the stopband center frequency, ω_c the 3 dB bandwidth frequency, Z_0 the characteristic impedance of the microstrip line, C the equivalent capacitance, L the equivalent inductance, and f_0 the resonance frequency.

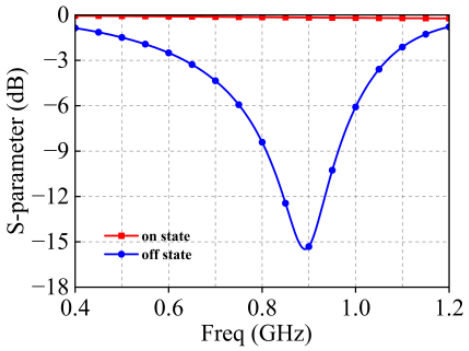

FIGURE 3. Transmission coefficient of the sensor in two states of the PIN diode.

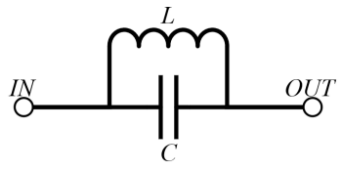

FIGURE 4. Equivalent circuit diagram of the sensor under forward bias of PIN diode.

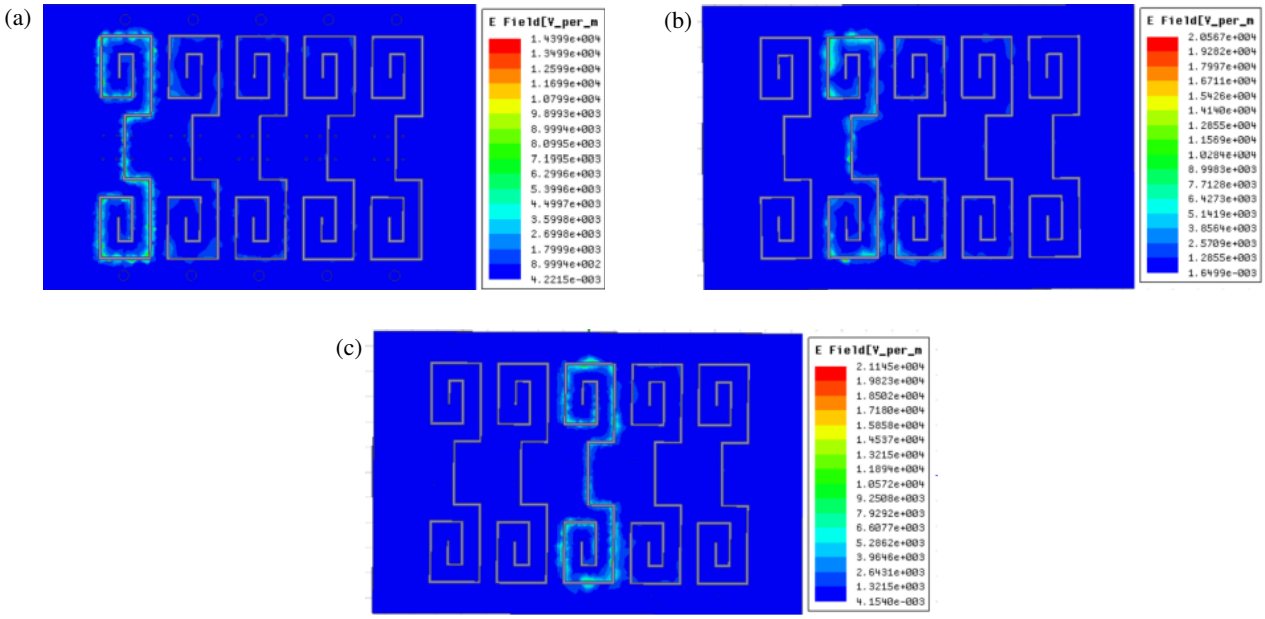

FIGURE 5. Electric field distribution diagram: (a) Electric field distribution diagram when detection unit 1 is in operation; (b) Electric field distribution diagram when detection unit 2 is in operation; (c) Electric field distribution diagram when detection unit 3 is in operation.

When L and C are in parallel resonance, the transmission coefficient (S_{21}) will exhibit a zero point. The resonance frequency at this point is given by:

$$f_0 = \frac{\omega_0}{2\pi} = \frac{1}{2\pi\sqrt{LC}} \tag{3}$$

Based on the above principles, if multiple DGS sensor units are cascaded into the same circuit, with each sensor unit responsible for detecting its respective region, it is possible to sequentially reconfigure each sensor unit through electronic control, thereby enabling defect detection across all regions. To testify the above hypothesis, five DGS sensor units were cascaded into a single circuit, and the simulated electric field distribution diagrams for selected cases are shown in Figure 5. The sensor detection units are labeled from left to right as unit 1, unit 2, and so on in each picture below.

Figure 5(a) shows the electric field distribution when the switch of sensor unit 1 is in the off state, and the other four switches are closed. Figures 5(b) and 5(c) follow in a similar manner. In Figure 5, we can clearly see that the region of concentrated field moves during the simulation. This phenomenon indicates that by changing the state of the PIN diodes, The region of field concentration can be controlled, which corresponds to the sensitive area of detection. Thanks to the physical structure of the spiral DGS, the field distribution becomes more uniformly, significantly reducing detection blind spots within a unit area. The detection area of each sensor unit is also enhanced, expanding the detection range and reducing the frequency of switching. Compared to traditional mechanical movement methods, the electronic control approach offers advantages of faster detection speed and lower motion errors. This control method is commonly referred to as "electronic scanning".

3. DEFECT SENSING PRINCIPLE

The presence of defects leads to a shift in resonance frequency. When a dielectric plate is loaded at the bottom of the sensor, it affects the DGS characteristics, increasing its capacitive component and causing the transmission zero to shift toward lower

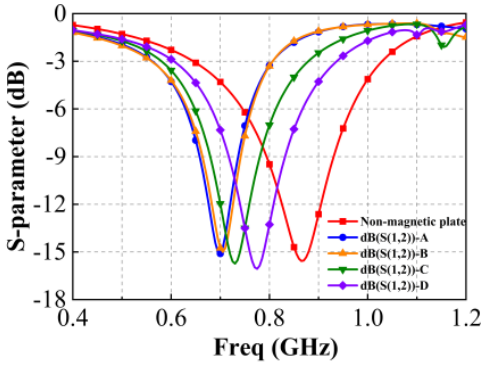

FIGURE 6. Electromagnetic simulation results (S_{21}).

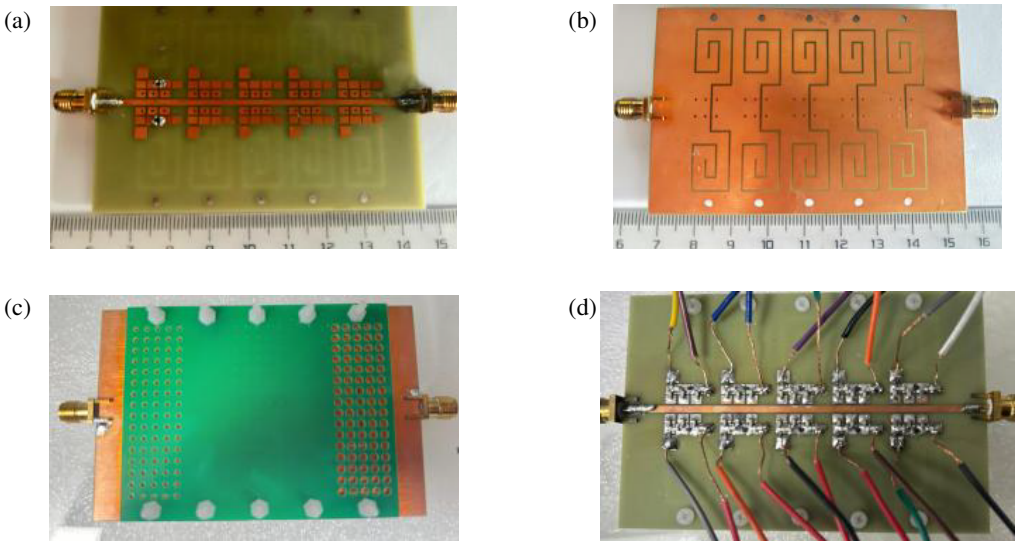

FIGURE 7. Physical image of the sensor: (a) Top view of the sensor circuit board; (b) Bottom view of the sensor; (c) Physical image of the sensor with the sample material loaded; (d) Physical image of the sensor with the biasing circuit loaded.

frequencies. Compared to a complete dielectric plate, a defective dielectric plate has a lower dielectric constant due to the defects. When a defective plate is loaded at the bottom of the DGS, although this also causes a shift in the transmission zero, the degree of this shift is smaller than that of the complete dielectric plate. Furthermore, the greater the number of defects is, the more significant the shift is, resulting in a larger difference in the position of the transmission zero than the complete plate. Therefore, by comparing the transmission zeros of the defective dielectric plate and the complete dielectric plate, defects can be effectively detected, and their severity can be assessed.

To validate this principle, we conducted a full simulation of the sensor's three-dimensional model in HFSS. The sensor retains the same geometric dimensions and substrate material as shown in Figure 2. In the simulation, an FR4 dielectric plate with dimensions of 56 mm $\times$ 30 mm $\times$ 1 mm was tightly fitted to the sensor, covering the entire DGS region. To verify the sensor's ability to effectively detect defects, we prepared dielectric plates with four different levels of defects for simulation and monitored the transmission coefficient of the sensor at various frequencies S_{21}.

The electromagnetic simulation results of the sensor with four different levels of defective dielectric plates and without a dielectric plate are shown in Figure 6. The defect levels of the four dielectric plates increase progressively, as shown in detail in Table 1. From Figure 6, it can be seen that the transmission zero occurs at 0.865 GHz without a dielectric plate. For the dielectric plates with different defect levels, the transmission zeros corresponding to defects A to D are 0.700 GHz, 0.705 GHz, 0.730 GHz, and 0.775 GHz, respectively. It is evident that as the defect severity increases, the shift in the transmission zero relative to the transmission zero of the non-defective dielectric plate becomes larger, which is consistent with our expectations.

4. TESTING AND VERIFICATION

To verify the above design, we created a sensor model based on the dimensions and materials specified in Section 2 and compared it with the simulation results. The physical photographs of the fabricated sensor are presented in Figure 7. Specifically, Figure 7(a) shows the top view of the sensor circuit board; Figure 7(b) illustrates the bottom view of the sensor; Figure 7(c) depicts the sensor with the sample material loaded; Figure 7(d)

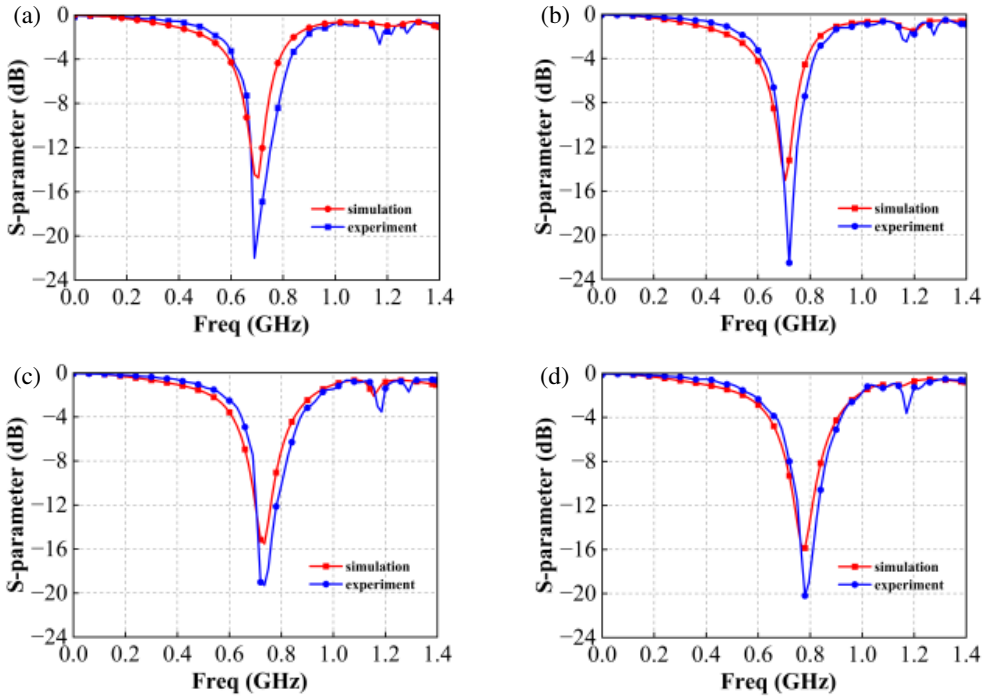

FIGURE 8. Comparison of measured and simulation results: (a) Comparison chart of class A defect results; (b) Comparison chart of class B defect results; (c) Comparison chart of class C defect results; (d) Comparison chart of class D defect results.

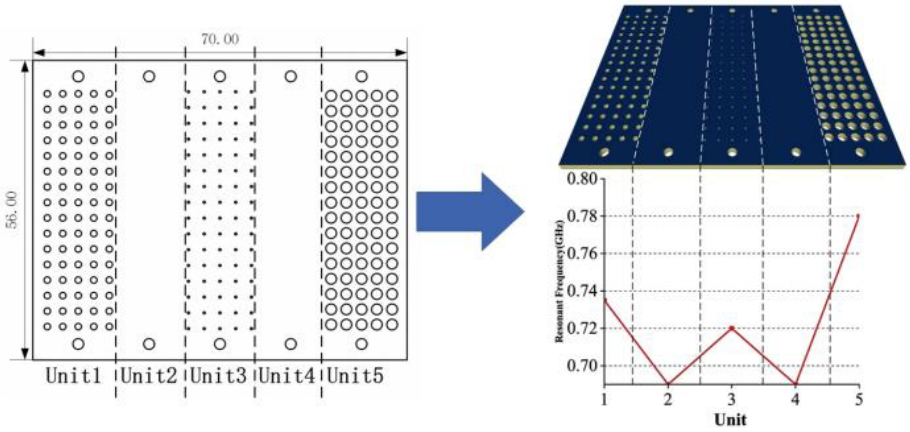

FIGURE 9. Schematic diagram of the dielectric plate detection unit (unit: mm).

displays the sensor with the biasing circuit loaded. We designed five holes on both the top and bottom of the sensor and fixed the dielectric sample with ten non-metallic screws. The parameters of the dielectric sample remain consistent with those in Section 3. STM32F103ZET6 microcontroller is used to control the switches of each detection unit of the sensor to achieve reconfigurability.

The comparison between the physical measurement and simulation results is shown in Figure 8. By comparing the simulation results with the actual measurement ones, we can observe significant consistency in the S-parameter curves. To provide a more intuitive comparison at the resonance frequency, we also compared the transmission zeros obtained from the simulation with the actual measurement results, aligning them with the transmission zeros of the five sensor units from left to right on the dielectric plate, and calculated the error. The measurement results are shown in Table 2, and the corresponding resonant frequencies of the units with different defect severities are illustrated in Figure 9.

As illustrated in Figure 9, there is a distinct correlation between the resonant frequencies of the sensor and the varying defect severities in each unit of the dielectric board. Defect Type A, representing the non-defective condition, is selected as the reference, and the resonant frequencies corresponding to each unit are recorded accordingly. It is clearly observed from Figure 9 that units 2 and 4 are free of defects, while the other three units show significant defects. Even a defect with a radius as small as 0.2 mm can be clearly identified through a measurable shift in the resonant frequency. By comparing the frequency deviations of the defective units with that of the non-

TABLE 1. Table of correspondence for dielectric slab defect numbering.

Types	Defect conditions of the dielectric plate
A	Defect-free
B	A circular defect with a diameter of 0.4 mm and a center-to-center spacing of 2.95 mm.
C	A circular defect with a diameter of 1.2 mm and a center-to-center spacing of 2.9 mm.
D	A circular defect with a diameter of 2 mm, and the center-to-center spacing is 2.85 mm.

TABLE 2. Comparison table of resonant frequency and simulation frequency for dielectric samples with different defect types.

Unitsss	Types	Simulation	Experiment	Error
		GHz	GHz	%
1	C	0.730	0.735	0.685%
2	A	0.700	0.690	0.709%
3	B	0.705	0.720	2.128%
4	A	0.700	0.690	0.709%
5	D	0.775	0.780	0.645%

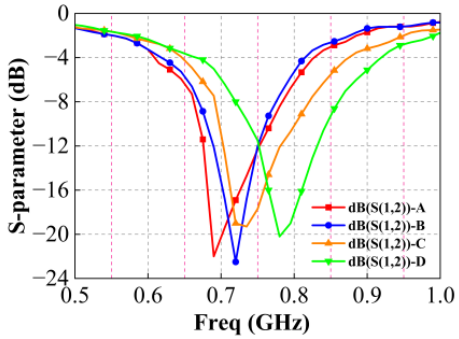

FIGURE 10. Comparison of measured results (S_{21}) for physical samples with dielectric slabs at different defect levels.

defective reference, the relative severity of the defects can be effectively estimated. This approach enables rapid and efficient detection of localized defects across different regions of the dielectric board through electronic control of the reconfigurable sensor.

Additionally, we compared the measurement results when loading dielectric samples with different types of defects, as shown in Figure 10. The experimental results also demonstrate a distinct nonlinear resonant behavior of the circuit. By leveraging the abrupt resonance shifts, defects can be effectively detected through monitoring of frequency deviations. The transmission zero frequencies for the four dielectric plates with different defect levels, labeled from A to D, are 0.690 GHz, 0.720 GHz, 0.735 GHz, and 0.780 GHz, respectively. As the defect level of the dielectric plate increases, the transmission zero frequency measured by the sensor shifts further from the transmission zero frequency of the non-defective dielectric plate, which is consistent with the electromagnetic simulation results shown in Figure 6.

5. CONCLUSION

This paper presents a defect scanning sensor based on reconfigurable DGS. The sensor's working principle was analyzed through electromagnetic simulations. When different defect levels of dielectric materials are loaded, compared to the transmission zero of a complete dielectric plate, the shift in the transmission zero is related to the level of defects. Leveraging the structural characteristics of the spiral DGS, the field distribution is more uniformly, effectively reducing detection blind spots. Through PIN diode control, the sensor dynamically modulates the electric field across different units, expanding the detection area of each unit. Compared to traditional mechanical movement and smaller detection units, this approach significantly enhances the detection speed. The experimental measurements show strong consistency with the simulation results, further validating the practical application of the proposed reconfigurable DGS-based sensor in defect detection.

REFERENCES

[1] Katnam, K. B., L. F. M. D. Silva, and T. M. Young, "Bonded repair of composite aircraft structures: A review of scientific challenges and opportunities," *Progress in Aerospace Sciences*, Vol. 61, 26–42, 2013.

[2] Cacciola, M., D. Pellicano, G. Megali, S. Calcagno, and F. C. Morabito, "Rotating electromagnetic field for NDT inspections," *Progress In Electromagnetics Research B*, Vol. 22, 305–320, 2010.

[3] Spyrou, E. D., T. Tsenis, and V. Kappatos, "Acousto-ultrasonic analysis of defects in composite specimens used in transportation domain," *Journal of Measurements in Engineering*, Vol. 9, No. 2, 117–127, 2021.

[4] Yan, Z. H., H. Xu, and P. F. Huang, "Multi-scale multi-intensity defect detection in ray image of weld bead," *NDT & E International*, Vol. 116, 102342, 2020.

[5] Zhang, T.-K., M.-H. Yu, K.-G. Dong, Y.-C. Wu, J. Yang, J. Chen, F. Lu, G. Li, B. Zhu, F. Tan, S.-Y. Wang, Y.-H. Yan, and Y.-Q. Gu, "Detector characterization and electron effect for laser-driven high energy X-ray imaging," *Acta Physica Sinica*, Vol. 66, No. 24, 245201, 2017.

[6] Hassan, O. S., M. S. u. Rahman, A. A. Mustapha, S. Gaya, M. A. Abou-Khousa, and W. J. Cantwell, "Inspection of antennas embedded in smart composite structures using microwave NDT methods and X-ray computed tomography," *Measurement*, Vol. 226, 114086, 2024.

[7] Foudazi, A., C. A. Edwards, M. T. Ghasr, and K. M. Donnell, "Active microwave thermography for defect detection of CFRP-strengthened cement-based materials," *IEEE Transactions on Instrumentation and Measurement*, Vol. 65, No. 11, 2612–2620, 2016.

[8] Arora, V. and R. Mulaveesala, "Pulse compression with gaussian weighted chirp modulated excitation for infrared thermal wave imaging," *Progress In Electromagnetics Research Letters*, Vol. 44, 133–137, 2014.

[9] Salim, A. and S. Lim, "Review of recent metamaterial microfluidic sensors," *Sensors*, Vol. 18, No. 1, 232, 2018.

[10] Li, Y. Y., Z. W. Deng, Y. Wang, Y. H. Xue, Y. B. Cao, Y. C. Liu, P. H. Zhao, W. J. Dang, W. L. Zhang, J. C. Li, J. S. Hao, and Q. F. Zeng, "Research progress on the principle and application of mndt of defects in nonmetallic materials," *NDT*, Vol. 48, No. 06, 1–7, 2024.

[11] Rahman, ur M. S., M. A. Abou-Khousa, and M. F. Akbar, "A review on microwave non-destructive testing (NDT) of composites," *Engineering Science and Technology, An International Journal*, Vol. 58, 101848, 2024.

[12] Balakrishnan, S. A., V. S. Ramalingam, E. F. Sundarsingh, A. Anbalagan, A. Ramachandran, W. Ahmed, S. Raman, and P. R, "Detection and characterisation of defects in composite materials using microwave non-destructive testing methods," *Proceedings of the Institution of Mechanical Engineers, Part C: Journal of Mechanical Engineering Science*, Vol. 238, No. 15, 7652–7660, 2024.

[13] Yeh, C. and R. Zoughi, "Microwave detection of finite surface cracks in metals using rectangular waveguides," *Research in Nondestructive Evaluation*, Vol. 6, No. 1, 35–55, 1994.

[14] Carrigan, T. D., B. E. Forrest, H. N. Andem, K. Gui, L. Johnson, J. E. Hibbert, B. Lennox, and R. Sloan, "Nondestructive testing of nonmetallic pipelines using microwave reflectometry on an in-line inspection robot," *IEEE Transactions on Instrumentation and Measurement*, Vol. 68, No. 2, 586–594, 2019.

[15] Yang, X., J. Chen, P. Su, X. Lei, J. Lei, Y. Xie, J. Yuan, and Z. Zhu, "Detection of defects in film-coated metals and non-metallic materials based on spoof surface plasmon polaritons," *IEEE Sensors Journal*, Vol. 19, No. 24, 11 891–11 899, 2019.

[16] Pendry, J. B., A. J. Holden, D. J. Robbins, and W. J. Stewart, "Magnetism from conductors and enhanced nonlinear phenomena," *IEEE Transactions on Microwave Theory and Techniques*, Vol. 47, No. 11, 2075–2084, 1999.

[17] Torun, H., F. C. Top, G. Dundar, and A. D. Yalcinkaya, "An antenna-coupled split-ring resonator for biosensing," *Journal of Applied Physics*, Vol. 116, No. 12, 124701, 2014.

[18] Boybay, M. S. and O. M. Ramahi, "Non-destructive thickness measurement using quasi-static resonators," *IEEE Microwave and Wireless Components Letters*, Vol. 23, No. 4, 217–219, 2013.

[19] Albishi, A. M., S. A. Alshebeili, and O. M. Ramahi, "Three-dimensional split-ring resonators-based sensors for fluid detection," *IEEE Sensors Journal*, Vol. 21, No. 7, 9138–9147, 2021.

[20] Tiwari, N. K., Y. Tiwari, and M. J. Akhtar, "Design of CSRR-based electronically tunable compact RF sensor for material testing," *IEEE Sensors Journal*, Vol. 18, No. 18, 7450–7457, 2018.

[21] Albishi, A. M., M. S. Boybay, and O. M. Ramahi, "Complementary split-ring resonator for crack detection in metallic surfaces," *IEEE Microwave and Wireless Components Letters*, Vol. 22, No. 6, 330–332, 2012.

[22] Albishi, A. M., "A novel coupling mechanism for CSRRs as near-field dielectric sensors," *Sensors*, Vol. 22, No. 9, 3313, 2022.

[23] Chen, J., J. Lei, P. Su, X. Lei, Y. Xie, Z. Zhu, J. Yuan, and X. Yang, "Detection of defects in non-metallic composite material based on electronically controlled spoof surface plasmon polaritons," *IEEE Sensors Journal*, Vol. 21, No. 3, 2883–2890, 2020.

[24] Wu, J., X. Yang, P. Su, W. Yu, and L. Zheng, "Defects detection method based on programmable spoof surface plasmon polaritons in non-metallic composites," *Micromachines*, Vol. 14, No. 4, 756, 2023.

[25] Buscarino, A., C. Famoso, L. Fortuna, and G. L. Spina, "Nonlinear jump resonance: Recent trends from analysis to electronic circuits implementations," *IEEE Transactions on Circuits and Systems II: Express Briefs*, Vol. 71, No. 3, 1727–1732, 2024.